

# An interactive mouthguard based on mechanoluminescence-powered optical fibre sensors for bite-controlled device operation

Received: 4 November 2021

Accepted: 23 August 2022

Published online: 10 October 2022

 Check for updates

Bo Hou<sup>1,7</sup>, Luying Yi<sup>1,7</sup>, Chao Li<sup>2,3</sup>, He Zhao<sup>1,4</sup>, Rong Zhang<sup>2</sup>, Bin Zhou<sup>2</sup>✉ and Xiaogang Liu<sup>1,4,5,6</sup>✉

Keyboards and touchscreens are widely used to control electronic devices, but these can be difficult to operate for individuals with dexterity impairments or neurological conditions. Several assistive technologies, such as voice recognition and eye tracking, have been developed to provide alternate methods of control. However, these can have problems in terms of use and maintenance. Here we report a bite-controlled optoelectronic system that uses mechanoluminescence-powered distributed-optical-fibre sensors that are integrated into mouthguards. Phosphors that are sensitive to mechanical stimulus are arranged in an array of contact pads in a flexible mouthguard; by using unique patterns of occlusal contacts in lateral positions, various forms of mechanical deformation can be distinguished by the fibre sensors via ratiometric luminescence measurements. By combining the device with machine learning algorithms, it is possible to translate complex bite patterns into specific data inputs with an accuracy of 98%. We show that interactive mouthguards can be used to operate computers, smartphones and wheelchairs.

Various technologies<sup>1–4</sup>—including voice recognition, eye-blink tracking, head-movement tracking, tongue-driven interaction and brain-computer interfaces—have been developed to help people control electronic devices<sup>5–12</sup>. However, many assistive technologies suffer problems in terms of device use and maintenance. For example, voice recognition requires a large operating memory, up-to-date hardware and low-noise operating environments<sup>5,6</sup>; eye tracking requires a camera to be mounted in front of the user and calibration is tedious and prone to fatigue<sup>7,8</sup>; and head-movement tracking excludes users with neurological conditions<sup>9,10</sup>. Brain-computer interfaces have

considerably improved in recent years<sup>11,12</sup>, but the technology requires the attachment of electrodes to the scalp for electroencephalogram, implantation under the skull for electrocorticogram or implantation in the brain for neural recording. This leads to cumbersome wired instrumentation and a high degree of invasiveness.

Bite force is often used as a parameter to assess masticatory function in dental research<sup>13,14</sup>. Dental occlusion provides high-precision control and requires minimal skill. As a result, a mouthguard containing integrated pressure sensors for detecting occlusal patterns and translating them into inputs could be a promising alternative

<sup>1</sup>Department of Chemistry, National University of Singapore, Singapore, Singapore. <sup>2</sup>Department of Precision Instruments, Tsinghua University, Beijing, China. <sup>3</sup>Aerospace Information Research Institute, Chinese Academy of Sciences, Beijing, China. <sup>4</sup>Joint School of National University of Singapore and Tianjin University, International Campus of Tianjin University, Binhai New City, Fuzhou, China. <sup>5</sup>National University of Singapore Suzhou Research Institute, Suzhou, China. <sup>6</sup>Institute of Materials Research and Engineering, Agency for Science, Technology and Research, Singapore, Singapore. <sup>7</sup>These authors contributed equally: Bo Hou, Luying Yi. ✉e-mail: [zhoub@mail.tsinghua.edu.cn](mailto:zhoub@mail.tsinghua.edu.cn); [chmlx@nus.edu.sg](mailto:chmlx@nus.edu.sg)

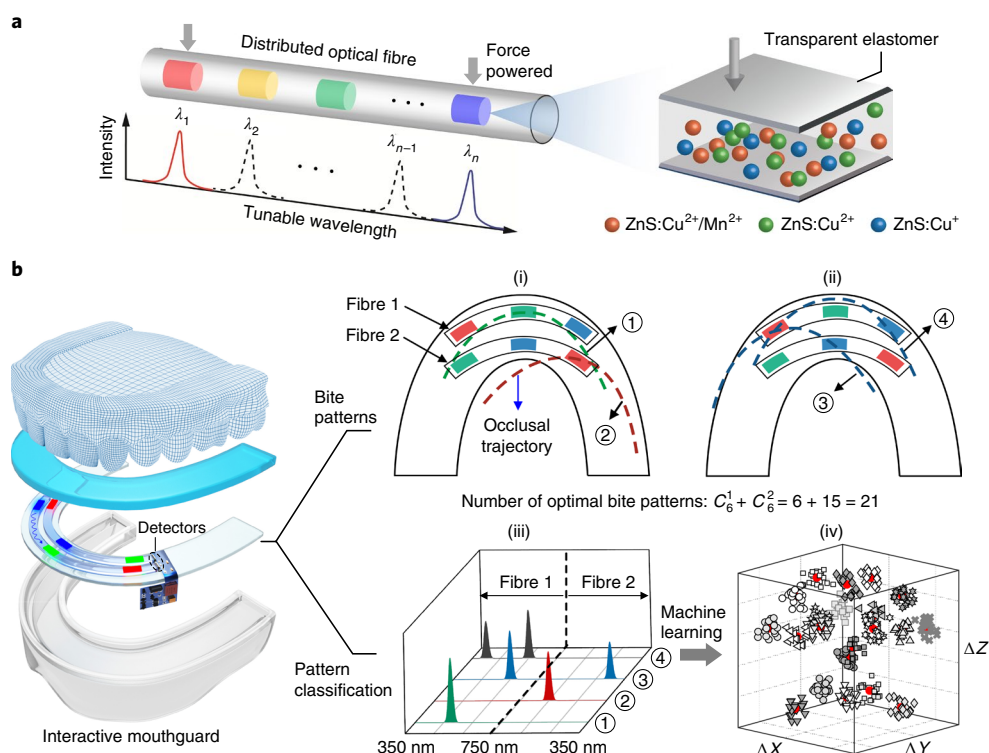


**Fig. 1 | Design of interactive mouthguard based on mp-DOF sensors.**

**a**, Schematic of mp-DOF comprising an elastomeric waveguide and embedded mechanoluminescent pads (ZnS:Cu<sup>2+</sup>/Mn<sup>2+</sup>, ZnS:Cu<sup>2+</sup> and ZnS:Cu<sup>+</sup> phosphors). **b**, Schematic of mp-DOF integration into a mouthguard. A 2 × 3 mp-DOF array comprising two sets of tricolour mechanoluminescent pads can theoretically generate 21 distinct patterns on biting one or two luminescent pads ( $C_6^1 + C_6^2 = 21$ ). Four bite patterns (①–④) are displayed (i and ii), where the dashed lines represent the typical contour of the upper teeth of an adult.

Fibres 1 and 2 input different optical spectra in the 350–750 nm range for each bite pattern (iii). Using machine learning, 21 complex occlusal patterns can be correctly identified according to the input CIE tristimulus values ( $X_1, Y_1, Z_1, X_2, Y_2$  and  $Z_2$ ) of the two fibres (iv). In (iv), the data for each pattern are labelled with the same symbol, and the red dots are the average chromaticity responses for each pattern. It should be noted that for display purposes, the scatter plot is drawn with coordinates ( $\Delta X = X_1 - X_2, \Delta Y = Y_1 - Y_2$  and  $\Delta Z = Z_1 - Z_2$ ).

to existing assistive technologies. This requires pressure sensors that are flexible, biocompatible, consume low power and allow distributed sensing. Stretchable optical pressure sensors, particularly distributed-optical-fibre (DOF) pressure sensors, are attractive for measuring occlusal patterns due to their high biocompatibility, lack of electromagnetic interference and their ability to monitor spatially distributed and time-dependent pressure along the transmission path of the fibre. However, existing fibre pressure sensors require an external light source, thereby increasing the system size and power consumption (Supplementary Table 1)<sup>4,15,16</sup>.

In this Article, we report mechanoluminescence-powered distributed-optical-fibre (mp-DOF) sensors that consist of an array of elastomeric waveguides embedded with mechanoluminescent contact pads containing different-coloured pressure-responsive phosphors. These sensors are integrated into mouthguards to create bite-controlled interactive telecommunication systems. Compression and deformation of the elastomeric mouthguard at specific segments during occlusion is mapped with the mp-DOF by measuring the intensity ratios of different colour emissions in the fibre system, without the need for external light sources<sup>15–19</sup>. Measurements of the ratiometric intensity of complex occlusal contacts can be processed using machine learning algorithms<sup>20</sup>, to convert into specific data inputs for high-accuracy remote control and operation of various electronic devices, including a computer, smartphone and wheelchair.

## Interactive mouthguard design

We designed an optical fibre with various transition-metal-doped zinc sulfide (ZnS) phosphors embedded at several predefined locations<sup>21–23</sup>

(Fig. 1a). Orange, green and blue mechanoluminescent emissions could be modulated by doping Cu<sup>2+</sup>/Mn<sup>2+</sup> (595 nm), Cu<sup>2+</sup> (525 nm) and Cu<sup>+</sup> (475 nm), respectively, into the ZnS host (Supplementary Fig. 1). The ZnS phosphors were chosen because of their intense mechanoluminescence, which does not require pre-irradiation and can be recovered. Beyond the primary colours, secondary colours could be produced by varying the composition of the three types of phosphor. When distributed compression was externally applied to the fibre, the mechanoresponsive phosphors emitted light at different wavelengths, which was propagated along the fibre by total internal reflection. This design principle was employed to fabricate an interactive mouthguard that comprised an integrated mp-DOF array, a flexible printed circuit board and a flexible polyethylene terephthalate substrate (Fig. 1b).

The developed interactive mouthguard can detect a variety of occlusal patterns. For example, a 2 × 3 mp-DOF array comprising two sets of tricolour mechanoluminescent pads can theoretically generate 21 distinct patterns when biting on one or two luminescent pads ( $C_6^1 + C_6^2 = 21$ ) (Supplementary Fig. 2). To design the occlusal patterns and make them as feasible as possible, we used the outlines of typical adult teeth during development. It should be noted that if more than two pads are bitten at once, more patterns will be generated; for example, three luminescent pads would generate  $C_6^1 + C_6^2 + C_6^3 = 41$ . Different occlusal trajectories give rise to mechanoluminescence with specific colour schemes, and the colour sensors record the CIE tristimulus values. A trained two-layer, feedforward artificial neural network (ANN) was developed to differentiate the 21 complex occlusal patterns in terms of tristimulus values ( $X_1, Y_1, Z_1, X_2, Y_2$  and  $Z_2$ ).

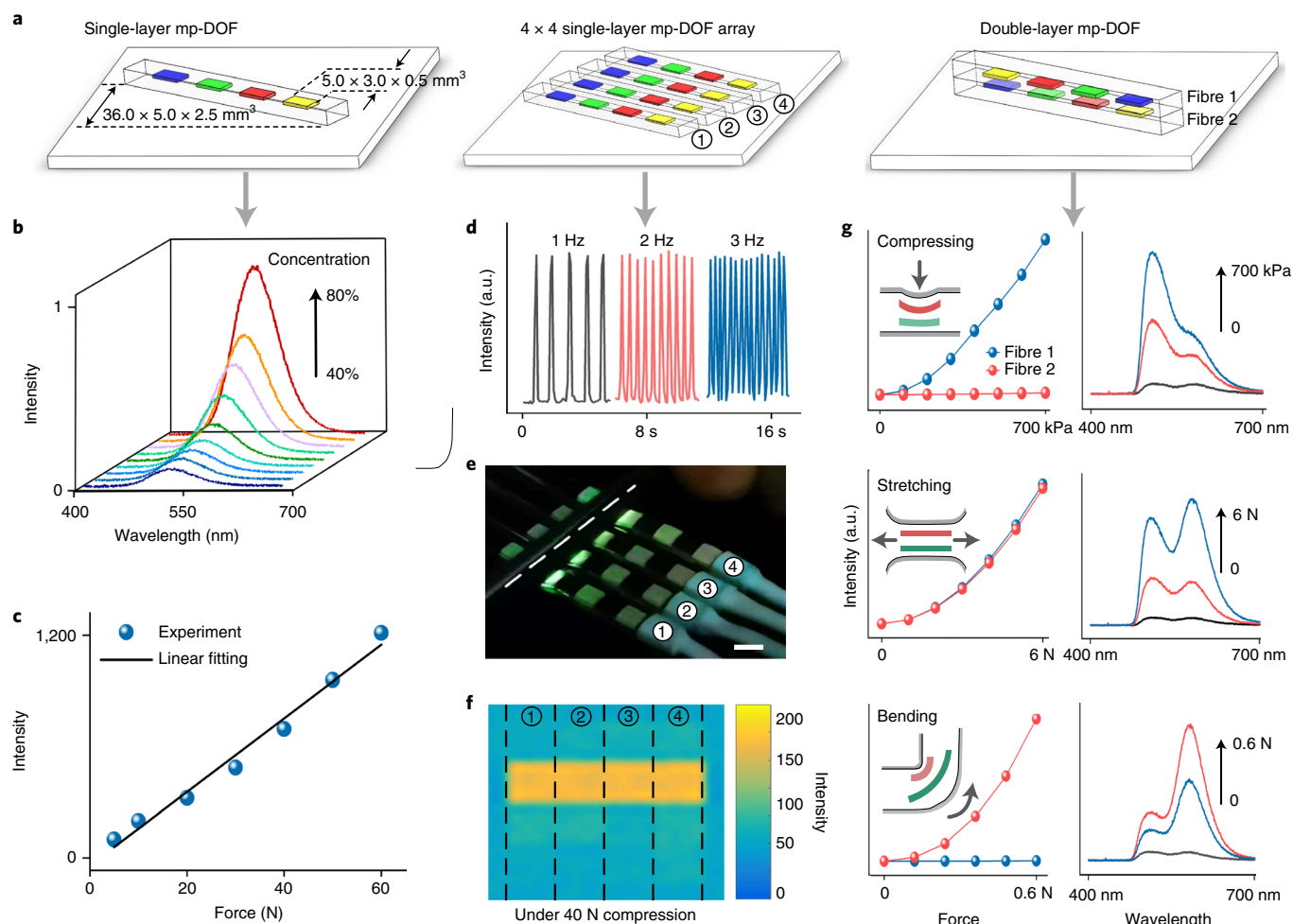


**Fig. 2 | Characterization of mp-DOF-based sensors in various configurations.**

**a**, Schematic of the mp-DOF sensor in three different configurations: a single-layer mp-DOF (left), a  $4 \times 4$  single-layer mp-DOF array to sense deformation (middle) and a double-layer mp-DOF to distinguish multiple deformations versus the luminous intensity of the optical fibre. **c**, Force sensitivity of the single-layer mp-DOF. **d**, Dynamic test of the mp-DOF at 1, 2 and 3 Hz. **e**, Optical

image of a single-layer  $4 \times 4$  mp-DOF array (**e**) and interface compression recorded under 40 N compression (**f**) through one-dimensional mechanical force projection (indicated by the dashed line in **e**). **g**, Optical power output (left) and corresponding spectra (right) of the double-layer mp-DOF on compression, stretching and bending. The insets depict the bilayer mp-DOF in different deformation modes.

## Characteristics and performance of mp-DOFs

We optimized the design of the mp-DOF sensors in various configurations, where mechanoluminescent materials were integrated into transparent optical waveguides (Fig. 2a and Supplementary Video 1). To ensure that the colour sensor collected the maximum optical power at one end of the fibres under low force, we studied the structure, key dimensions and composition of the materials for mp-DOFs (Supplementary Fig. 3). Considering the light collection efficiency and ease of processing, each mechanoluminescent pad was optimized with dimensions of  $5.0 \times 3.0 \times 0.5$  mm, aligned parallel to one another along the fibre axis. The dimensions of the fibre were  $36.0 \times 5.0 \times 2.5$  mm. Replica moulding was employed to fabricate the mp-DOF sensors (Supplementary Fig. 4). We investigated the luminescence behaviour of the mechanoluminescent pads with ZnS:Cu<sup>2+</sup>/Mn<sup>2+</sup> particles of different concentrations (Fig. 2b). The force sensitivity of the mp-DOF was tested by plotting the integral intensity as a function of the external force, and the intensity increased approximately linearly in the range of 5–60 N (Fig. 2c and Supplementary Fig. 5). The force sensitivity defined by the curve slope was 20 counts per newton (integrated time, 0.25 s; Fig. 2c), which was sufficient to identify the bite patterns. Moreover, the dynamic characteristics of the mp-DOF

was investigated by compressing the optical fibre at various frequencies (1, 2 and 3 Hz), demonstrating a highly stable and reproducible signal output (Fig. 2d). Mechanoluminescence had a time resolution of approximately 52.6 ms. The robustness of the mp-DOF was tested by applying compression over 2,000 cycles, and the intensity difference was within 5.5%. We also examined the temperature characteristics of the mp-DOF, and its luminescence fluctuation remained within 3.7% from 20 to 50 °C.

We next characterized the performance of both single-layer and double-layer mp-DOF sensors. The single-layer sensor measured the distributed mechanical force, whereas the double-layer sensor could differentiate between diverse force modes, such as stretching, bending and compression (Supplementary Video 1). Compression maps were obtained using a  $4 \times 4$  single-layer mp-DOF array under different force patterns (Fig. 2e,f and Supplementary Fig. 6). Furthermore, we performed stretching, compression and bending tests to evaluate the stress distribution and light propagation of the double-layer mp-DOF sensor. As the mechanoluminescent pads embedded in the upper and lower fibres emitted light at different wavelengths, the mode and magnitude of the applied force could be spectroscopically distinguished. The detected power  $P$  of fibre 1 was larger than, approximately equal

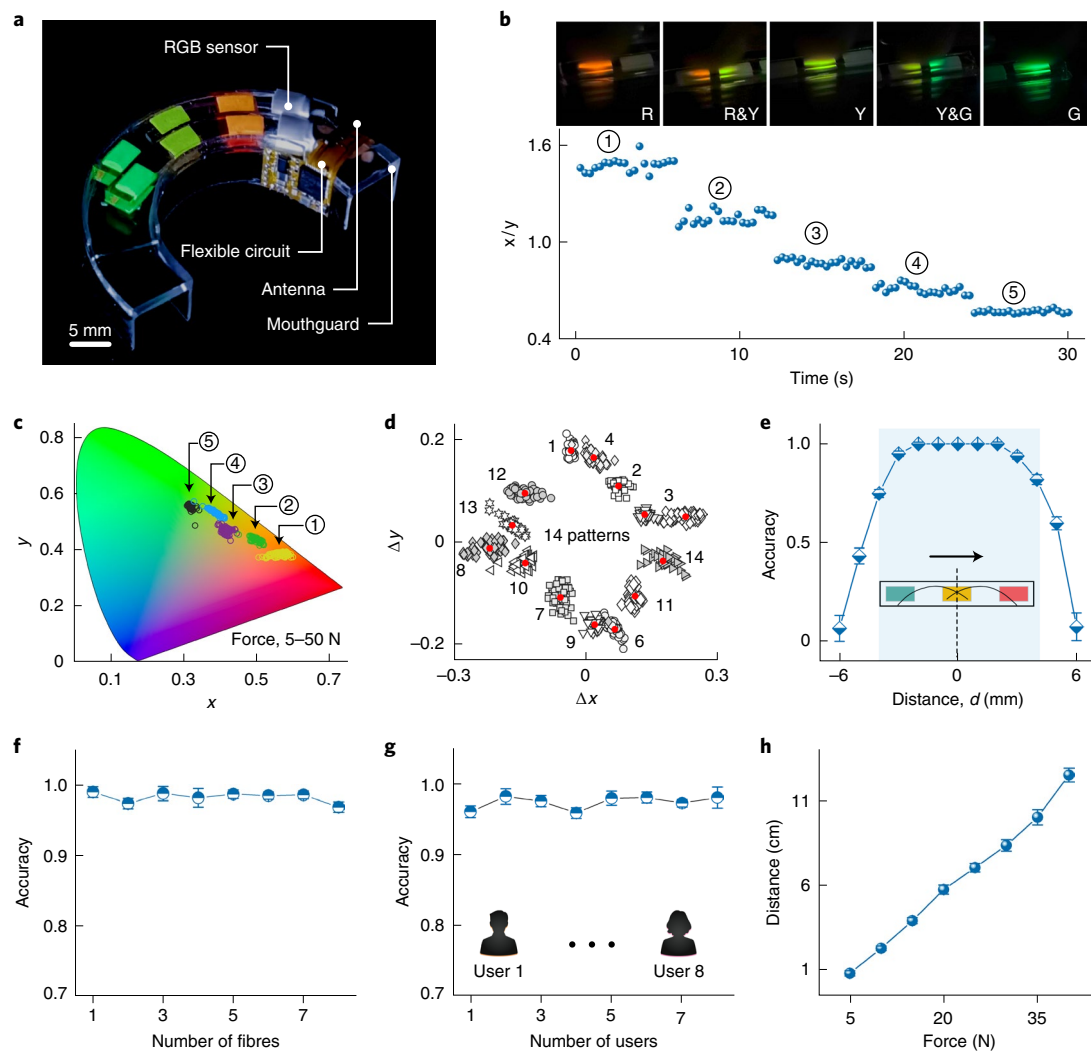


**Fig. 3 | Evaluation of mp-DOF-integrated interactive mouthguard.**

**a**, Photograph of the integrated device comprising an elastomer mouthguard, a bilayer array of multicolour contact pads and a flexible circuit module.

**b**, Normalized real-time chromaticity response in  $x/y$  coordinates, derived from five occlusal trajectories comfortable to users. The insets are the corresponding photographs of the mp-DOF under five force patterns. **c**, Chromaticity response of five occlusal patterns under different forces (5–50 N). **d**, Classification results of 14 occlusal patterns detected by a  $2 \times 3$  mp-DOF array using machine learning algorithms.  $\Delta x = x_1 - x_2$  and  $\Delta y = y_1 - y_2$ . The data for each pattern are labelled with

the same symbol, and the red dots are the average chromaticity responses for each pattern. **e**, Bite position versus classification accuracy as measured using a tricolour mp-DOF. The inset depicts the bite movement path around the centre of the mp-DOF. **f**, Classification accuracy for different  $2 \times 3$  mp-DOF arrays. The same user uses different mp-DOFs to bite 14 patterns multiple times, and the collected data were fed into an ANN for classification. **g**, Classification accuracy of bite patterns for random users. **h**, Linear relationship between the mouse-cursor movement distance and biting force, recorded when controlling a mouse cursor. The error bars represent the standard deviation for each point.

to and smaller than that of fibre 2 in the compression, stretching and bending modes, respectively. We simulated the magnitude of the first principal stress received by the luminescent pads and the fibre's transmission efficiency under three different mechanical stimuli (Supplementary Fig. 7). In theory, the optical power  $P$  at the end of each fibre is given by the formula  $P = aE^2S$ , where  $a$  is the proportionality factor,  $E$  is the first principal stress value of the mechanoluminescent pad and  $S$  is the light transmission efficiency of the optical waveguide. The experimental results corroborate the numerical results. Therefore, combining these two fibres in a double-layer configuration yielded marked changes in spectral output across all the three modes of deformation (Fig. 2g). Compared with previously reported mechanoluminescent sensors, mp-DOF can detect mechanical force magnitudes and recognize multiple mechanical stimuli, which can be further developed for applications including joint motion recognition, skin tactile perception and facial recognition<sup>24–27</sup>.

## Technical evaluation of integrated interactive mouthguards

To construct a mechanoluminescence-assisted interactive mouthguard, we integrated a  $2 \times 3$  single-layer mp-DOF sensor array with six compression points into a three-dimensionally printed soft mouthguard (Fig. 3a). The right lateral, medial and left lateral compression points of the mp-DOF were covered with ZnS:Cu<sup>2+</sup>/Mn<sup>2+</sup> (595 nm emission), ZnS:Cu<sup>2+</sup>/Mn<sup>2+</sup>–ZnS:Cu<sup>2+</sup> (595 and 525 nm emission with equal intensity) and ZnS:Cu<sup>2+</sup> (525 nm emission) particles, respectively. Two high-sensitivity colour sensor chips (detection limit, 0.5 pW cm<sup>-2</sup>) were placed at the end of the mp-DOF and connected to a flexible processing circuit. The circuit has a thickness of 80 μm and could be effectively bent to fit well inside the mouthguard. The interactive mouthguard's circuit includes colour sensor chips, a Bluetooth 5.0 system on a chip and power management chips (Supplementary Fig. 8). The circuit size is  $9 \times 12$  mm and the total power consumption is 9.09 mW.

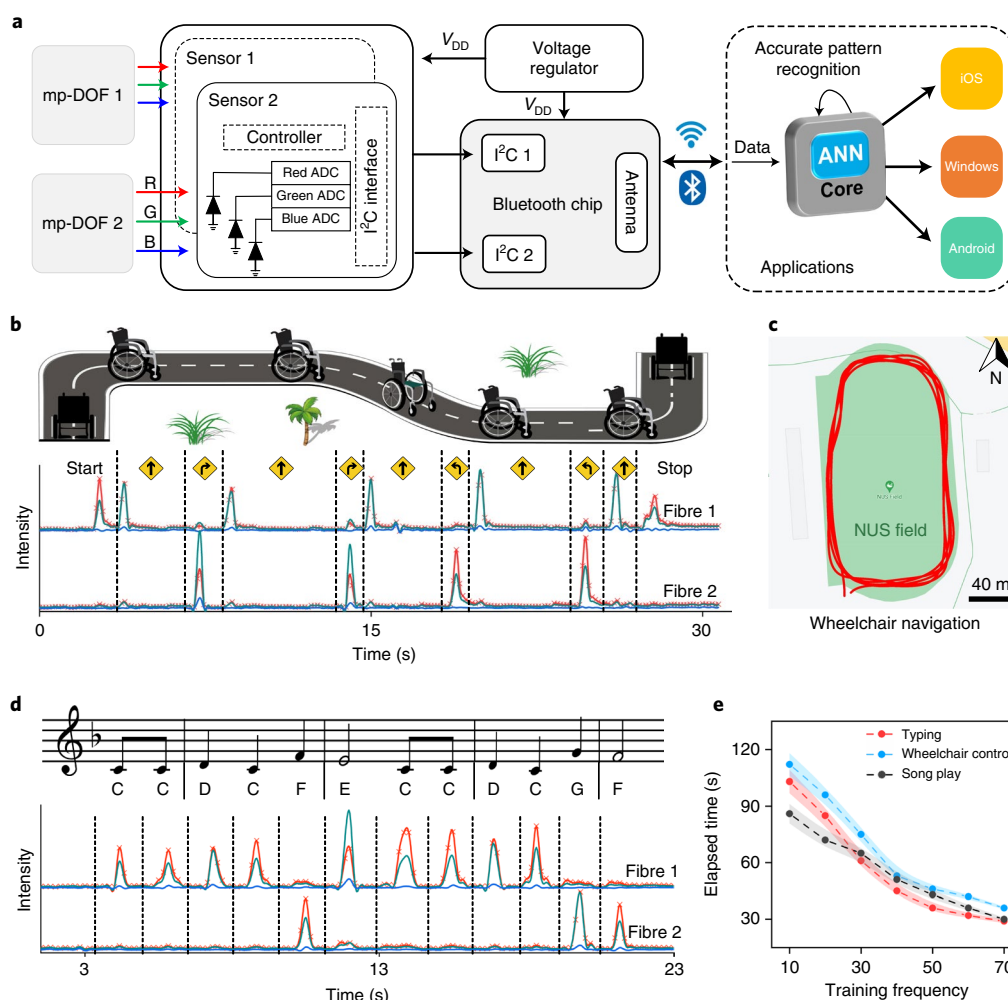


**Fig. 4 | Interactive mouthguard with a  $2 \times 3$  mp-DOF array for assistive technology demonstration.** **a**, Flow chart for interactive mouthguard control. Two RGB sensors detect the spectrum data from two fibres with different occlusion patterns and convert them into digital signals for Bluetooth-chip-controlled external devices. External devices integrated with the ANN algorithm judge the occlusal pattern instruction from incoming data to take appropriate action. ADC, analogue-to-digital converter.  $V_{DD}$  is the operating voltage of the digital circuit. **b**, Wheelchair navigation using the mouthguard. The motion trajectory of the wheelchair and the corresponding real-time emission profiles

are presented. **c**, Monitoring wheelchair navigation around a standard 400 m running track (five repeated runs) using the global positioning system. Scale bar, 40 m. **d**, Playing a virtual piano using the mouthguard. A temporally ordered sequence of musical notes for Happy Birthday and the corresponding emission profiles are presented. The red, green and blue curves in **b** and **d** represent the tristimulus values  $X$ ,  $Y$  and  $Z$ , respectively. The output spectra of fibres 1 and 2 correspond to the various occlusal patterns shown in Supplementary Fig. 9. **e**, Total time spent to complete each task versus training frequency for wheelchair control, song playing and typing.

The mouthguard prototype is 48 mm long, 26 mm wide and 12 mm high, and its total weight is less than 7 g. The mouthguard and mp-DOF were made of elastomers, and metal components such as circuits were sealed with elastomeric polydimethylsiloxane (PDMS).

To distinguish occlusal patterns, we converted the  $X$ ,  $Y$  and  $Z$  tristimulus values of the colour sensor into the CIE  $xyY$  colour space (Methods provides more details on occlusal pattern identification). We first normalized the  $x/y$  chromaticity response in real time into five comfortable bite patterns that could be distinguished with each fibre (Fig. 3b). The plotted chromaticity response data of the five occlusal patterns in the force range of 5–50 N demonstrated that pattern identification could be achieved by comparing variations across the chromaticity space (Fig. 3c). On the colour diagram, the chromaticity responses of identical patterns do not coincide at any point. This is due to changes in the occlusal position and the mechanical force sensitivity of mechanoluminescent materials. However, as long as the position error and force dynamic range are within the permitted range, it is still possible to discern between various patterns. Given that five patterns

were accurately distinguished using one fibre, it was possible to differentiate 20 patterns ( $2C_3^5 + C_3^2$ ) using two fibres. We used 14 occlusal patterns for interactive bite-controlled operation (Supplementary Fig. 9), after considering the adaptive comfort of the users. Machine learning was used to identify the occlusion pattern based on the output spectra of these 14 occlusal patterns (Fig. 3d).

Instead of common machine learning algorithms such as decision trees (DTs) and support vector machines (SVMs), an ANN was used to process complex patterns due to its improved precision, accuracy and robustness. The trained feedforward ANN recognized 14 patterns with an accuracy greater than 98% (Supplementary Fig. 10). We explored the relationship between the recognition accuracy and bite position offset  $d$  (Fig. 3e). The classification accuracy reached 100% when biting the centre of the middle pad and decreased as the biting position moved away from the centre. Within a distance of 8 mm, the accuracy remained greater than 75% (Fig. 3e, within the light-blue-shaded area). To further evaluate the accuracy of the system, eight pairs of mp-DOFs were tested, and all of them had a classification accuracy greater than

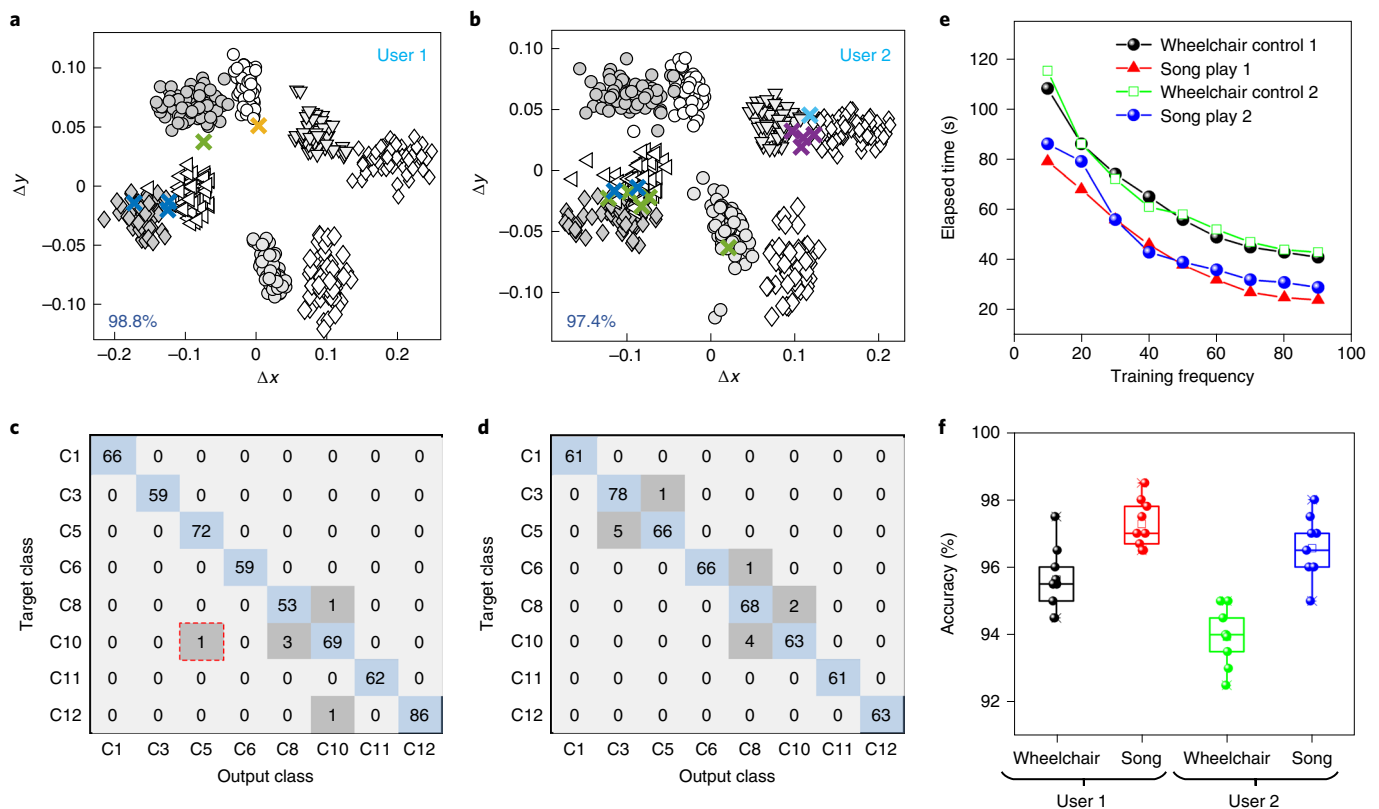


**Fig. 5 | Efficacy of the ANN-based interactive mouthguard using occlusal data from two users on specific tasks. a, b,** Chromatic response distribution of eight bite patterns from user 1 (**a**) and user 2 (**b**) during multiple plays of the tune of Happy Birthday. The data for different occlusal patterns are marked with different labels, and points marked with 'x' are the data that were misidentified. **c, d,** Confusion matrices corresponding to classification results of **a** (**c**) and **b** (**d**). The numbers in the dark-grey boxes indicate the number of misidentified data.

For example, number 1 marked with a red dashed box in **c** means that the user intended to bite on pattern 10, but the actual bite pattern was identified by the ANN as pattern 5; such misidentification occurred once. The numbers in blue boxes on the diagonal indicate the amount of accurately identified data. **e,** Total time spent by different users to complete each task versus training frequency. **f,** Control accuracy for the two users on different tasks.

97% (Fig. 3f). Eight participants were invited to test this interactive system, and the recognition accuracy of each pattern remained greater than 96.5% (Fig. 3g).

We next investigated the separate roles of luminance and emission intensity in expanding the boundary processing for interactive control. Although the chromaticity of the mechanoluminescent pads remained unchanged under different forces, the mechanoluminescence intensity was proportional to the magnitude of the force. This feedback endowed the mp-DOF sensors with an additional input variable beyond chromaticity (Supplementary Video 2). A participant was able to demonstrate opening a specific user interface, such as a web browser or music streaming application, by bite-controlled cursor movements where the cursor movement distance could be precisely controlled by adjusting the amplitude of bite force (Fig. 3h), with a control accuracy of 98.3%. For the interaction with an on-screen keyboard, the sorting between the function specification and bite patterns is illustrated in Supplementary Fig. 11, in which the magnitude of bite force determines the movement steps. The participant controlled the bite interface to accurately type the letter keys 'LOVE' and number keys '3.14' using the virtual keyboard in less than 32 s (Supplementary Video 2). The average typing speed was 22 characters per minute, comparable to the typing speed (13–30 characters per minute) of existing brain–computer interface technologies<sup>11</sup>.

### Interactive mouthguards for assistive technology

By pairing the interactive mouthguard with a Bluetooth module, real-time bite patterns can be classified and sent to an external device

for performing appropriate actions, or to a custom mobile application for data display and collecting (Fig. 4a and Supplementary Fig. 12). For example, users can connect the phone application to make emergency calls by biting the mouthguard with specific occlusal trajectories (Supplementary Fig. 11). Our interactive mouthguard can also function as a remote-control handle, such as for remote control of a wheelchair (Fig. 4b and Supplementary Video 3). With the addition of the Bluetooth module, users can control the wheelchair to turn, speed and brake, as well as to navigate around a standard 400 m running track (Fig. 4c and Supplementary Fig. 13). Validation tests revealed that the interactive mouthguard had a response time of less than 0.12 s. Moreover, we demonstrated the use of our system to control a custom-made virtual keyboard to play the tune of 'Happy Birthday' (Supplementary Video 3), and part of the output light signals are presented in Fig. 4d. When the sensor was bitten, the signal processing algorithm was used to classify the captured luminescence signals and convert them into corresponding musical notes, with a dwell time of 0.2 s. The average time to complete each note was less than 0.8 s, with an accuracy of 98.2%. Notably, the mouthguard is easy to use; after 70 training sessions, a high level of mouthguard proficiency can be achieved (Fig. 4e).

### Efficacy test of ANN-based interactive mouthguard on specific tasks

We also evaluated the efficacy of the ANN-algorithm-based interactive mouthguard on specific tasks using occlusal data from two different mouthguard users. Two participants wore interactive mouthguards to operate the wheelchair and play the tune of Happy Birthday, and

the completion time of each task was recorded. After the participants mastered the operation, 100 sets of occlusal data were collected to train various classification models suitable for different users (Fig. 5a–d). For example, due to different tooth shapes and occlusal habits, two participants need different chromaticity classification boundaries to identify eight occlusal patterns when controlling the on-screen keyboard with the mouthguard. After 70 training sessions, both participants can control the wheelchair and keyboard with proficiency (Fig. 5e). Using the ANN, participant 1 could control the wheelchair and virtual keyboard with an average accuracy of 95.5% and 97.2%, respectively, and participant 2 could control the wheelchair and virtual keyboard with an average accuracy of 94.2% and 96.7%, respectively (Fig. 5f).

## Conclusions

We have reported an interactive mouthguard for the bite-controlled operation of computers, smartphones and wheelchairs. The mouthguard uses contact pads containing mechanical-stimulus-sensitive phosphors that emit in different colours when compressed and mp-DOF sensors to detect the optical signal generated by different occlusal patterns of the wearer. When combined with machine learning, the DOF sensors enable the accurate recognition of complex bite patterns for electronic device operation, whereas the luminescence intensity can be easily decoupled from chromaticity as another controllable parameter. The mouthguards are light (weighing under 7 g), compact, use biocompatible materials and offer high force sensitivity and precision control with minimal training experience (compared with existing assistive technologies). Although the current prototype is designed for well-aligned teeth, mouthguards with an irregular arrangement of mechanoluminescent pads could be created for users with different teeth patterns or who wear dentures. The mp-DOF sensors are also an extremely durable transducer that can reduce energy consumption and promote a more sustainable optoelectronic system. Unlike conventional electronic pressure sensors<sup>28–30</sup>, luminescence-based pressure sensors are less susceptible to electromagnetic interference. However, it should be noted that although parts of the mouthguard that come into contact with human skin (such as PDMS and polyurethane elastomers) are considered biocompatible, they must still be tested for compliance with relevant medical device standards before use.

## Methods

### Materials

**Material characterization.** Mechanoluminescent phosphors of ZnS:M (M = Mn<sup>2+</sup> or Cu<sup>2+</sup>)@Al<sub>2</sub>O<sub>3</sub> particles were purchased from LONCO. The phosphor size (~28 μm on average) and morphology were characterized using a scanning electron microscope (Tecnai G2F20 S-TWIN, FEI Nano Ports). The sample composition was determined by energy-dispersive X-ray spectroscopy operated with a Bruker model A300 spectrometer. X-ray powder diffraction was performed using an X-ray powder diffractometer (D/MAX-3C, Rigaku).

**Mechanoluminescence mechanism.** Mechanoluminescence of ZnS:Mn microparticles is probably governed by piezoelectricity and photoexcitation effects. On applying strain, the trapped electrons escape into the conduction band of ZnS. The electrons recombine with hole centres or transfer to the valence band and cause non-radiative energy release, with some transferring to activated Mn<sup>2+</sup> ions. The excited Mn<sup>2+</sup> ion falls back to its ground state and emits orange light. The emission peak around 585 nm is generated by the <sup>4</sup>T<sub>1</sub>(<sup>4</sup>G) → <sup>6</sup>A<sub>1</sub>(<sup>6</sup>S) transition.

When ZnS:Cu particles are stimulated by an external force, plastic deformation leads to band bending. Subsequently, electrons trapped in the shallow donor level tunnel to the conduction band. When these electrons recombine with holes, green and blue emission occurs (Supplementary Fig. 1)<sup>31–36</sup>.

## Design and fabrication of mp-DOFs

**Basic design considerations for constructing mp-DOFs.** The mp-DOFs were fabricated by embedding mechanoluminescent phosphors (ZnS:M) into an elastic matrix to form a waveguide. The light collection efficiency critically depended on the shape and size of the fibres.

Total internal reflection in the optical fibres results from the difference in the refractive index between the core and cladding materials. When light travels from an optically dense medium to a less dense medium, total internal reflection occurs when the incident angle of the incident light to the core boundary is larger than the critical angle, which is expressed as follows:

$$\sin(\varphi_c) = \frac{n_1}{n_2}, \quad (1)$$

where  $\varphi_c$  is the critical angle and  $n_2$  and  $n_1$  are the refractive indices of the core and cladding materials, respectively. Only those emissions at an incident angle larger than  $\varphi_c$  can be transmitted through the fibre by total internal reflection.

### Comparison of light collection efficiency between square and tapered optical fibres.

For a square optical fibre whose cross-sectional area at the incident end ( $S_i$ ) is equal to that at the exit end ( $S_e$ ), the ratio of power at the exit end ( $P_f$ ) to the power at the luminescent source ( $P_s$ ) is as follows:

$$\frac{P_f}{P_s} = \frac{2\beta}{360^\circ} = \frac{180^\circ - 2\varphi_c}{360^\circ}, \quad (2)$$

where  $\beta$  is the collection angle.

When light propagates in a tapered optical fibre ( $S_i \neq S_e$ ), the incident angle  $\phi$  of each reflection is as follows:

$$\phi = 90^\circ - \beta + (2m - 1)\alpha, \quad (3)$$

where  $m$  is the number of reflections and  $\alpha$  is the cone angle.

For a positively tapered optical fibre ( $S_i < S_e$ ),  $\alpha > 0$ . From equation (3), we know that the incident angle  $\phi$  is increased by  $2\alpha$  for each reflection, allowing the light with the first reflection angle larger than  $\varphi_c$  to be transmitted (that is,  $90^\circ - \beta + \alpha \geq \varphi_c$ ); thus,

$$\frac{P_f}{P_s} = \frac{2\beta}{360^\circ} = \frac{180^\circ - 2\varphi_c + 2\alpha}{360^\circ}. \quad (4)$$

For a negatively tapered optical fibre ( $S_i > S_e$ ),  $\alpha < 0$ . The incident angle is reduced by  $|\alpha|$  for each reflection, allowing the light with the last reflection angle larger than  $\varphi_c$  to be transmitted (that is,  $90^\circ - \beta + (2m - 1)\alpha \geq \varphi_c$ ); thus,

$$\frac{P_f}{P_s} = \frac{2\beta}{360^\circ} = \frac{180^\circ - 2[\varphi_c + (2m - 1)|\alpha|]}{360^\circ}. \quad (5)$$

The light transmission efficiency of the three types of optical fibre under mechanical deformation was simulated using commercial finite element analysis software (COMSOL Multiphysics v5.6).

**Dimensional analysis of mp-DOFs.** The mp-DOF was designed as a rectangular waveguide (width  $W \times$  height  $H \times$  length  $L$ ) embedded with a rectangular mechanoluminescent pad ( $W_1 \times H_1 \times \text{Len}$ ). The location of the luminescent pad in the waveguide is denoted as ( $W_2, H_2$ ), where  $W_2$  and  $H_2$  are the differences in the centre coordinates between the luminescent pad and waveguide in the width and thickness directions, respectively. The spacing between the luminescence cores is denoted as  $L_d$ . We next theoretically analyse the light collection efficiency, which depends on the size of the fibres.

First, we consider the luminescent pad to be two dimensional, that is,  $L_{en} = 0$ . According to the imaging theory used for fibre optics, for a square optical fibre, any ray that emanates from the real source and is reflected by a surface is geometrically equivalent to an undeviated ray from a virtual source. A virtual source is identical to the real source, and they are symmetrical about the reflected surface. Multiple reflections off all the four fibre walls generate a two-dimensional array of virtual sources in the input plane. We wish to determine the illuminance at a given position  $P$  in the output plane of the fibre, which is equivalent to the process of tracing the ray back to the virtual light source array in the input plane. Therefore, power ( $P_p$ ) at point  $P$  is actually the integral of the power density of the virtual light sources in a circle with radius  $l_b \tan \varphi_c$  centred at point  $P$ , that is,

$$P_p = \int_0^{2\pi} \int_0^{l_b \tan \varphi_c} S(r, \theta) r dr d\theta, \quad (6)$$

where  $l_b$  is the distance from the virtual light source plane to the output plane,  $(r, \theta)$  are the polar coordinates in the input plane and  $S(r, \theta)$  is the power density function of the virtual light source array in the circle. In the mp-DOF, a two-dimensional virtual light source array is composed of many large rectangles with size  $W \times H \times L$  whose sides are adjacent. Inside each large rectangle is a small rectangle with a size of  $W_1 \times H_1 \times L_{en}$ . Because only power  $S$  in the small rectangle representing each luminescent pad is equal to  $S_0$  and  $S = 0$  for the area around the small rectangles, the integral in equation (6) is approximately the area of all the small rectangles within the circle. Each virtual source in the array is indicated using a pair of indices  $(m, n)$ , and equation (6) can be written as follows:

$$P_p(x_0, y_0) = S_0 \int_0^{\varphi_c} \sum_{m,n} \int_{mW+W_2+x_0}^{mW+W_2+W_1+x_0} \int_{nH+H_2+y_0}^{nH+H_2+H_1+y_0} dx dy d\varphi \quad (7)$$

$$(0 \leq x^2 + y^2 \leq l_b \tan \varphi) \quad 0 \leq x_0 \leq W, 0 \leq y_0 \leq H$$

where  $(x, y)$  are the coordinates of the virtual light source plane and  $(x_0, y_0)$  are the coordinates of the output plane;  $\varphi$  is the incident angle of each ray. Considering that the length of each luminescent pad is  $L_{en}$ , power  $P_p$  from the three-dimensional luminescent pad is the integral of equation (7) in the interval  $[0, L_{en}]$  in the length direction. Equation (7) is applicable to every luminescent pad in the mp-DOFs.

We analysed the relationship between the size of mp-DOFs and the light collection efficiency using COMSOL Multiphysics. The multiphysics model consisted of ray optics and solid-state physics. The main parameters include the following: length  $L_{en}$  and width  $W_1$  of the mechanoluminescent pad, distance between each pad  $L_d$ , width  $W$  and thickness  $H$  of the optical fibre, and position  $H_2$  of the mechanoluminescent pad in the thickness direction of the fibre. First, the thickness of the mechanoluminescent pad was set to 500  $\mu\text{m}$  because a thicker pad would exhaust the light and prevent transmission. We chose  $M_{\text{fibre}} > M_{\text{pad}}$  to prevent optical attenuation due to soft fibre deformation. When  $M_{\text{fibre}} > M_{\text{pad}}$ , the luminous efficiency is higher when the mechanoluminescent pad is near the fibre's surface. Considering fibre service time and luminescence efficiency, we placed the pad in the middle of the fibre. Considering occlusal accuracy and detected intensity at the fibre end, width  $W_1$  of the mechanoluminescent pad was set to 3.0 mm; length and interval, to 5.0 mm; and width and thickness of the fibre, to 5.0 mm and 2.5 mm, respectively (Supplementary Fig. 3).

**Selection of elastomeric material for mp-DOFs.** Because the elastomeric materials used for the mp-DOFs must efficiently transmit force and light simultaneously, their mechanical and optical properties must be considered. The criteria for selecting materials for waveguide production include a large difference in refractive index between the core and cladding as well as high transparency. The mechanical properties

of the elastomers used in the mechanoluminescent pad and waveguide must be simultaneously considered. For ease of description, Young's modulus of the elastomeric materials used in the mechanoluminescent pad and waveguide are denoted as  $M_{\text{pad}}$  and  $M_{\text{guide}}$ , respectively. It was demonstrated that mechanoluminescence intensity exhibits an approximate quadratic relation to  $M_{\text{pad}}$  (ref. 33). Therefore,  $M_{\text{core}}$  must be large. The luminous intensity of the luminescent pad is proportional to the average first principal stress applied to it. Therefore, we simulated and analysed the average first principal stress on the luminescent pad when compression (500 kPa) was applied to the waveguide with different Young's moduli. The results indicated that greater the difference between  $M_{\text{pad}}$  and  $M_{\text{guide}}$ , the greater is the average first principal stress applied to the luminescent pad. Since a greatly deformed waveguide with small  $M_{\text{guide}}$  under mechanical force causes severe optical attenuation, an elastomeric material with larger  $M_{\text{guide}}$  was selected to construct the optical fibre. To choose elastomeric materials for mp-DOF, we included a list of commercially available elastomeric materials in Supplementary Table 2 (refs. 37–40).

**Fabrication of mp-DOFs.** In our design, the mp-DOF was a 36 mm rectangular fibre with a cross section of 2.5 mm (height) by 5.0 mm (width). ZnS:M phosphors were doped into silica gel (parts A and B were mixed at a 10:1 ratio) for fabrication of the mechanoluminescent pad, and the mass ratio of ZnS:M to silica gel was 8:2. The optical fibre was fabricated by a simple moulding process. First, the luminescent pad was produced by injecting evenly mixed ZnS:M phosphors and silica gel into a rectangular bar (5.0  $\times$  3.0  $\times$  0.5 mm) through a syringe and leaving it to thermally cure at 80  $^\circ\text{C}$  for approximately 30 min. Thereafter, the mixed silicone LS-6946 (parts A and B were mixed at a 10:1 ratio) was applied to the luminescent pad to form half the transparent waveguide. Then, demoulding of the solidified fibre was performed and the other half of the transparent waveguide was cast using silicone LS-6946. The waveguide was thermally cured at 70  $^\circ\text{C}$  for approximately 30 min. Finally, two coating steps were employed. The first was to cover the surface damage of the waveguide during demoulding using silicone LS-6946, whereas the second was to fabricate the cladding of the optical fibre by coating PDMS (SYLGARD 184; parts A and B were mixed at a 10:1 ratio) on the fibre and curing it in a 70  $^\circ\text{C}$  oven for 30 min. The thickness of the cladding was 200  $\mu\text{m}$  (Supplementary Fig. 4).

**Force sensitivity of mp-DOF.** The mp-DOF has a layer of mechanoluminescent phosphors and a transparent transmission layer. We simplify the fibre into two coaxial cylinders (luminescent material layer and transparent transmission layer). According to Lamé's formula, the relationship between fibre strain and applied force can be established. When a cylinder with a multilayered slender structure is subjected to the radial pressure exerted from the outside, the relationship between the radial, axial and circumferential stress and strain of each layer is expressed as

$$\begin{bmatrix} \varepsilon_r(n) \\ \varepsilon_\theta(n) \\ \varepsilon_z(n) \end{bmatrix} = \begin{bmatrix} \lambda(n) + 2\mu(n) & \lambda(n) & \lambda(n) \\ \lambda(n) & \lambda(n) + 2\mu(n) & \lambda(n) \\ \lambda(n) & \lambda(n) & \lambda(n) + 2\mu(n) \end{bmatrix}^{-1} \times \begin{bmatrix} \sigma_r(n) \\ \sigma_\theta(n) \\ \sigma_z(n) \end{bmatrix}, \quad (8)$$

where  $n$  represents the number of layers. Here  $\sigma_r(n)$ ,  $\sigma_\theta(n)$  and  $\sigma_z(n)$  represent the radial, circumferential and axial stresses of the  $n$ th layer structure, respectively. Also,  $\varepsilon_r(n)$ ,  $\varepsilon_\theta(n)$  and  $\varepsilon_z(n)$  are the radial, circumferential and axial strains of the  $n$ th layer structure, respectively. Furthermore,  $\lambda(n)$  and  $\mu(n)$  are the first and second Lamé parameters of the  $n$ th layer material, respectively, which can be determined by the following formulas:

$$\lambda(n) = \frac{\nu_n \times E_n}{(1 + \nu_n)(1 - 2\nu_n)}, \mu(n) = \frac{E_n}{2(1 + \nu_n)}, \quad (9)$$

where  $E_n$  and  $\nu_n$  represent the elastic modulus and Poisson's ratio of the  $n$ th layer material, respectively.

Therefore, the axial strain of the luminescent material layer under pressure  $P$  can be obtained as

$$\varepsilon_z(1) = \frac{2\nu_1 P}{E_1}. \quad (10)$$

When the fibre sensor is subjected to pressure, according to the shear lag theory, shear stress is generated at the interface between the transparent transmission layer and phosphor layer; therefore, the axial strain of the phosphor layer is

$$\Delta\varepsilon = \rho \frac{2\nu_a/E_a - 2\nu_b/E_b}{\left[1 + \frac{\pi r^2}{h\omega - \pi r^2} \times \frac{E_b}{E_a}\right]}, \quad (11)$$

where  $E_a$  and  $\nu_a$  represent the elastic modulus and Poisson's ratio of the transparent transmission material, respectively;  $E_b$  and  $\nu_b$  are the elastic modulus and Poisson's ratio of the mechanoluminescent phosphor layer, respectively. Also,  $r$  represents the radius of the emission layer and  $h$  and  $\omega$  are the thickness and width of the transmission layer, respectively.

According to equations (10) and (11), the axial strain generated by the emission layer under radial pressure  $P$  can be obtained as

$$\varepsilon = \varepsilon_z(1) + \Delta\varepsilon = \frac{2\nu_b P}{E_b} + \rho \frac{2\nu_a/E_a - 2\nu_b/E_b}{\left[1 + \frac{\pi r^2}{h\omega - \pi r^2} \times \frac{E_b}{E_a}\right]}. \quad (12)$$

Therefore, sensitivity  $k_p$  of fibre pressure sensor is expressed as

$$k_p = \frac{2\nu_b}{E_b} + \frac{2\nu_a/E_a - 2\nu_b/E_b}{\left[1 + \frac{\pi r^2}{h\omega - \pi r^2} \times \frac{E_b}{E_a}\right]}. \quad (13)$$

### Performance evaluation of mp-DOFs

**Force response test.** To measure the force response, we used a z-axis stage to repeatedly press a force gauge onto the mp-DOF with a force of 5–30 N in 5 N increments (Supplementary Fig. 5). The real-time force was measured by the force gauge. The light emission was collected using a spectrometer (Ocean Optics QE Pro). Using a fibre optic spectrometer, the light intensity is obtained by integration over time, which is proportional to the exposure time. The force response was tested with an integration time of 128 ms.

**Temperature response test.** The setup for the temperature response test was the same as that used for the force response test, except that the mp-DOF was placed on a heating plate with a digital display. A compression force of 15 N was applied to the green-emitting pad, and the temperature was increased from 20 to 50 °C in 10 °C increments.

**Dynamic test.** The response time of the mp-DOF was explored using a z-axis stage to repeatedly and quickly press the force gauge onto the fibre. A fibre optic spectrometer and force gauge were used to record the luminescence and force, respectively. The integration time of the spectrometer was 50 ms.

**Cyclic fatigue test.** A cyclic extension experiment was conducted on a customized mechanical motion platform that could cyclically stretch the fibre. The two frequency-controlled electric translation stages repeatedly moved towards and away from each other to achieve repeated stretching of the optical fibre. Light emission was collected from the fibre's side using the spectrometer. The mechanoluminescent pad mixed with ZnS:Cu<sup>2+</sup> and ZnS:Mn<sup>2+</sup>/Cu<sup>2+</sup> was measured for

2,000 cycles. A compression cycle test was performed using a z-axis stage to repeatedly compress a force gauge onto the mp-DOF with a force of 30 N, and light emission was collected using the spectrometer. The bending cycle test was conducted by placing the mp-DOF between two parallel stages: one is fixed and the other moving back and forth in controlled increments. After 2,000 cycles of compression, tensile and bending tests, the difference in luminous intensity was within 5.5%, 5.1% and 6.3%, respectively.

### Simulation for multifunctional sensing

The mechanism of a multifunctional soft sensor composed of a double-layer mp-DOF was simulated using COMSOL Multiphysics, which indicated that the sensor was capable of distinguishing the deformation modes of compression, stretching and bending. The simulated structure included two layers of mp-DOFs, separated by a layer of opaque medium with Young's modulus of 0.5 MPa. The light transmittance of the luminescent pad was 5%, and Young's moduli of the luminescent pad and waveguide were 2.0 and 1.5 MPa, respectively. The size of the luminescent pad was 0.5 mm × 3.0 mm × 6.0 mm, and the length of the optical fibre was 16.0 mm. For ease of description, the upper fibre and embedded luminescent pad are referred to as fibre 1 and pad 1, respectively, and the lower fibre and embedded luminescent pad are referred to as fibre 2 and pad 2, respectively. On pressing, the average principal stress on pad 1 ( $E_1$ ) was much larger than that on pad 2 ( $E_2$ ), and the optical transmission rate of fibre 1 ( $S_1$ ) was also larger than that of fibre 2 ( $S_2$ ). Under tensile force,  $E_1 \approx E_2$  and  $S_1 \approx S_2$ . When the fibre was bent upwards,  $E_1 < E_2$  and  $S_1 < S_2$  (Supplementary Fig. 7).

### Tests of multifunctional soft sensor

**Compression response test.** A double-layer mp-DOF was pressed using the same setup and configuration as those employed for the force response measurements described in the 'Performance evaluation of mp-DOFs' section. Two colour sensors connected to the fibres measured the light intensity of each fibre. The spectrometer was placed in the middle of the double-layer mp-DOF end to measure the spectrum.

**Stretching response test.** A double-layer mp-DOF was stretched on a customized linear translation stage, similar to the setup used in the cyclic extension test described in the 'Performance evaluation of mp-DOFs' section. One end of the fibre was fixed, whereas the other end was connected to a reciprocating linear translation stage.

**Bending response test.** A double-layer mp-DOF was placed between two parallel stages. One stage was fixed, whereas the other moved forward in controlled increments, causing bending of the luminescent pad in the fibre. The tensile force in the forward direction of the stage was measured with a force gauge.

### Circuit design and characteristics

Because the mp-DOFs are mechanoluminescence powered with zero power consumption, the main sources of system power consumption are the colour sensor (AS73211), power supply chip (TLV62569) and Bluetooth chip (DA14585). AS73211 is an integrated colour sensor with low power consumption (3.0 V, 1.5 mA) and low noise. It achieves an accuracy of up to 24 bit signal resolution with an irradiance responsivity of 0.5 pW cm<sup>-2</sup>. To achieve stable, high-precision measurements, the digital and analogue grounds of the circuit were divided, and the power supply was equipped with a large capacitor to reduce circuit noise as much as possible. The sensor was connected to DA14585 via I<sup>2</sup>C. DA14585 integrating an ARM Cortex-M0 microcontroller is a 5.0 Bluetooth chip with low power consumption, -20 dB transmission sensitivity and -93 dB receiver sensitivity. Four AS73211 sensors were connected to a Bluetooth chip by sharing the I<sup>2</sup>C interface address. The working voltage was 3.0 V. The working current of the Bluetooth transceiver was 3 mA and the working time was 10 ms s<sup>-1</sup>. Thus, the

total average power consumption of the interactive mouthguard under normal operating conditions was calculated to be 9.09 mW.

To reduce the size of the device, we selected a small lithium battery ( $10.0 \times 10.0 \times 1.6$  mm) as the power supply, with a battery capacity of 60 mAh. When the interactive mouthguard operates with real-time data processing and Bluetooth communication, the entire system can continue to work for approximately 24 h without recharging the battery.

All the circuit components were arranged on a flexible printed circuit board with a thickness of 80  $\mu\text{m}$ . The size of the main circuit was  $9.0 \times 12.0 \times 1.6$  mm, and the circuit was completely embedded in the mouthguard. The largest circuit component was the Bluetooth chip ( $5 \text{ mm} \times 5 \text{ mm}$ ). The weight of two mp-DOFs was 1.2 g, and the weight of the flexible circuit board was 0.2 g. The weight of the battery was 1.2 g, and the total weight of the interactive mouthguard was 2.6 g. Thermal images of the circuit board revealed that circuit heating did not exceed  $1^\circ\text{C}$  after 90 min of operation. Moreover, the electromagnetic radiation intensity of the circuit was equivalent to that of mobile phones (Supplementary Fig. 8).

### Integration and assembly of interactive mouthguard

After the processed mp-DOFs and colour sensors were interconnected, they were connected to the Bluetooth chip on the circuit board by a thin flexible wire, and the Bluetooth chip transmitted data to mobile phones or personal computers. Then, the entire system was integrated into a mouthguard made of thermoplastic polyurethane elastomer. Thermoplastic polyurethane has excellent comprehensive properties such as high strength, high toughness, abrasion resistance and oil resistance, and is widely used in medical, food and other industries. To facilitate biting, a convex plate was provided at the upper position of the corresponding luminescent pad so that users could determine the bite position more flexibly and accurately. The PDMS elastomer used to seal circuit components such as batteries is biocompatible, transparent at optical frequencies and mechanically robust.

### Occlusal pattern identification

The raw data included six CIE spectral tristimulus values from two colour sensors:  $X_1, X_2, Y_1, Y_2, Z_1$  and  $Z_2$ . To increase the classification accuracy, we converted  $X, Y$  and  $Z$  tristimulus values into the CIE xyY colour space:

$$x = \frac{X}{X+Y+Z}, y = \frac{Y}{X+Y+Z}. \quad (14)$$

Fourteen patterns that were comfortable for biting were selected to develop the applications. Therefore, the goal of the processing algorithm was to determine which of the 14 patterns the current bite pattern belonged to based on four input values ( $x_1, x_2, y_1$  and  $y_2$ ). The results processed using threshold evaluation, DT, SVM and ANN algorithm were compared.

The threshold evaluation algorithm simply preset the threshold value of each input signal. The DT, SVM and ANN algorithm were in the built-in application toolboxes of MATLAB 2021b: Classification Learner and Neural Pattern Recognition. For the ANN, a two-layer feedforward neural network comprising sigmoid hidden and SoftMax output neurons was used. This neural network had an input layer of four nodes. The output layer consisted of 14 nodes, and the SoftMax function was used to predict one estimated state among the 14 states. There was a hidden layer between the input and output layers with ten nodes. The activation function used was the sigmoid function. The SVM algorithm was a quadratic SVM model with a quadratic polynomial kernel function, and the DT algorithm was a fine tree model.

The participants wore the smart mouthguard integrated with a  $2 \times 3$  mp-DOF array and 14 bit patterns to obtain a dataset. There were more than 300 data points for each pattern. After being preprocessed using equation (8), 75% of the data were fed into each algorithm for training. The trained models were used to identify the remaining 25% of the data.

The classification accuracy of the threshold evaluation was 89.0%. Threshold evaluation is relatively simple; however, it has low accuracy and is difficult to apply to flexible interactions. Moreover, it is difficult to directly and independently set the threshold, making machine learning a necessity. With accuracy rates of 98.4% and 98.0%, respectively, the ANN and SVM had advantages, and the ANN was selected as the classification algorithm for prototype development (Supplementary Fig. 10).

### Prototype applications

**Designing mouse and keyboard functions.** For the mouse function, the up, down, left, right, left-click and right-click functions of a mouse corresponded to bite patterns 3, 8, 6, 10, 1 and 11, respectively. In addition, the navigation distance was defined according to the amplitude of the bite force and luminous intensity. We used the interactive mouthguard to open, use and close a web browser. For the keyboard function, the up, down, left, right, enter, and switch between alphabetic and numeric keyboard functions corresponded to bite patterns 3, 8, 6, 10, 1 and 5, respectively. To test the accuracy and efficiency of the keyboard function, we created a Microsoft Word document, and then repeatedly wrote the word 'LOVE' and number '3.14' (Supplementary Fig. 11). The duration to complete the input of all the characters did not exceed 32 s (the duration was from the time the participant activated the keyboard until the last character was entered).

**Designing virtual keyboard.** We designed an on-screen keyboard with a total of ten keys. The tune Happy Birthday containing eight notes could be played using the keyboard. Bite patterns 5, 3, 1, 10, 8, 6, 11 and 12 corresponded to musical notes C, D, E, F, G, A, B and C (high), respectively. When subjected to biting, the sensor captured the input signal and performed classification. It then directed the keyboard to play the corresponding note.

**Designing wheelchair navigation.** The wheelchair used was a standard electrical wheelchair (W5517, Inuovo). Bite patterns 3, 8, 10 and 6 corresponded to the forward, backward, turning left and turning right functions, respectively, and bite pattern 5 controlled switching between starting and braking. Wheelchair control was achieved using the Bluetooth interface. During operation, occlusal pattern data were first transmitted to the computer via Bluetooth chips. After the data were classified and processed, the corresponding action command was sent to the wheelchair via another Bluetooth chip. The circular and figure-of-eight complex trajectories of the wheelchair controlled by biting demonstrated the flexibility of the system, and five tests on the same trajectory revealed the stability of the system.

**Customized mobile phone application design.** A smartphone application (App) was designed to operate with the interactive mouthguard and provide a user-friendly interface for data display and collection. To use this application, the user should first put on the interactive mouthguard and open the App installed on the smartphone, and then establish a secure Bluetooth connection between the App and mouthguard. Subsequently, the App can receive and display the data stream from the mouthguard in real time. The App is capable of plotting a graph of these data streams versus time during the user's physical activity. Data and graphs can be stored on the device, uploaded to cloud servers online and shared via social media. Additionally, with the App, users can make emergency calls through different bite patterns (Supplementary Fig. 12). The current implementation was programmed in the Android environment, and similar application interfaces can be developed for other operating systems, such as iOS.

### Data availability

The data that support the plots within this paper and other findings of the study are available from the corresponding authors upon reasonable request.

## Code availability

The code is available from the corresponding authors upon reasonable request.

## References

- Yu, X. et al. Skin-integrated wireless haptic interfaces for virtual and augmented reality. *Nature* **575**, 473–479 (2019).
- Zhou, Z. et al. Sign-to-speech translation using machine-learning-assisted stretchable sensor arrays. *Nat. Electron.* **3**, 571–578 (2020).
- Bouton, C. E. et al. Restoring cortical control of functional movement in a human with quadriplegia. *Nature* **533**, 247–250 (2016).
- Bai, H. D. et al. Stretchable distributed fiber-optic sensors. *Science* **370**, 848–852 (2020).
- Cao, W. J. et al. Voice controlled wheelchair integration rehabilitation training and posture transformation for people with lower limb motor dysfunction. *Technol. Health Care* **29**, 609–614 (2021).
- Pei, J. et al. Towards artificial general intelligence with hybrid Tianjic chip architecture. *Nature* **572**, 106–111 (2019).
- Jin, P., Zou, J., Zhou, T. & Ding, N. Eye activity tracks task-relevant structures during speech and auditory sequence perception. *Nat. Commun.* **9**, 5374 (2018).
- Oyama, A. et al. Novel method for rapid assessment of cognitive impairment using high-performance eye-tracking technology. *Sci. Rep.* **9**, 12932 (2019).
- Lee, H., Park, S. H., Yoo, J. H., Jung, S. H. & Huh, J. H. Face recognition at a distance for a stand-alone access control system. *Sensors* **20**, s20030785 (2020).
- Guo, H. Y. et al. A highly sensitive, self-powered triboelectric auditory sensor for social robotics and hearing aids. *Sci. Robot.* **3**, eaat2516 (2018).
- Nuyujukian, P. et al. Cortical control of a tablet computer by people with paralysis. *PLoS ONE* **13**, e0204566 (2018).
- Willett, F. R., Avansino, D. T., Hochberg, L. R., Henderson, J. M. & Shenoy, K. V. High-performance brain-to-text communication via handwriting. *Nature* **593**, 249–254 (2021).
- Kim, J. et al. Wearable salivary uric acid mouthguard biosensor with integrated wireless electronics. *Biosens. Bioelectron.* **74**, 1061–1068 (2015).
- Verma, T. P., Kumathalli, K. I., Jain, V. & Kumar, R. Bite force recording devices—a review. *J. Clin. Diagn. Res.* **11**, ZE01–ZE05 (2017).
- Kim, T. et al. Heterogeneous sensing in a multifunctional soft sensor for human-robot interfaces. *Sci. Robot.* **5**, eabc6878 (2020).
- Xu, P. A. et al. Optical lace for synthetic afferent neural networks. *Sci. Robot.* **4**, eaaw6304 (2019).
- Li, G. et al. Self-powered soft robot in the Mariana Trench. *Nature* **591**, 66–71 (2021).
- Guo, J., Zhou, B., Yang, C., Dai, Q. & Kong, L. Stretchable and temperature-sensitive polymer optical fibers for wearable health monitoring. *Adv. Funct. Mater.* **29**, 1902898 (2019).
- Lindsey, N. J., Dawe, T. C. & Ajo-Franklin, J. B. Illuminating seafloor faults and ocean dynamics with dark fiber distributed acoustic sensing. *Science* **366**, 1103–1107 (2019).
- Butler, K. T., Davies, D. W., Cartwright, H., Isayev, O. & Walsh, A. Machine learning for molecular and materials science. *Nature* **559**, 547–555 (2018).
- Qian, X. et al. Printable skin-driven mechanoluminescence devices via nanodoped matrix modification. *Adv. Mater.* **30**, 1800291 (2018).
- Du, Y. et al. Mechanically excited multicolor luminescence in lanthanide ions. *Adv. Mater.* **31**, 1807062 (2019).
- Zhao, Y. et al. Multiresponsive emissions in luminescent ions doped quaternary piezophotonic materials for mechanical-to-optical energy conversion and sensing applications. *Adv. Funct. Mater.* **31**, 2010265 (2021).
- Wang, X. et al. Dynamic pressure mapping of personalized handwriting by a flexible sensor matrix based on the mechanoluminescence process. *Adv. Mater.* **27**, 2324–2331 (2015).
- Zhang, J. et al. Flexible and stretchable mechanoluminescent fiber and fabric. *J. Mater. Chem. C* **5**, 8027–8032 (2017).
- Pan, C. et al. High-resolution electroluminescent imaging of pressure distribution using a piezoelectric nanowire LED array. *Nat. Photon.* **7**, 752–758 (2013).
- Zhao, X. et al. Self-powered user-interactive electronic skin for programmable touch operation platform. *Sci. Adv.* **6**, eaba4294 (2020).
- Araromi, O. A. et al. Ultra-sensitive and resilient compliant strain gauges for soft machines. *Nature* **587**, 219–224 (2020).
- Leber, A. et al. Soft and stretchable liquid metal transmission lines as distributed probes of multimodal deformations. *Nat. Electron.* **3**, 316–326 (2020).
- Zhao, S. & Zhu, R. Electronic skin with multifunction sensors based on thermosensation. *Adv. Mater.* **29**, 1606151 (2017).
- Chen, B., Zhang, X. & Wang, F. Expanding the toolbox of inorganic mechanoluminescence materials. *Acc. Mater. Res.* **2**, 364–373 (2021).
- Chandra, V. K., Chandra, B. P. & Jha, P. Self-recovery of mechanoluminescence in ZnS:Cu and ZnS:Mn phosphors by trapping of drifting charge carriers. *Appl. Phys. Lett.* **103**, 161113 (2013).
- Moon Jeong, S., Song, S., Lee, S.-K. & Choi, B. Mechanically driven light-generator with high durability. *Appl. Phys. Lett.* **102**, 051110 (2013).
- Qasem, A., Xiong, P., Ma, Z., Peng, M. & Yang, Z. Recent advances in mechanoluminescence of doped zinc sulfides. *Laser Photonics Rev.* **15**, 2100276 (2021).
- Wang, F. et al. Mechanoluminescence enhancement of ZnS:Cu,Mn with piezotronic effect induced trap-depth reduction originated from PVDF ferroelectric film. *Nano Energy* **63**, 103861 (2019).
- Zhuang, Y. & Xie, R. J. Mechanoluminescence rebrightening the prospects of stress sensing: a review. *Adv. Mater.* **33**, e2005925 (2021).
- Martincek, I., Pudis, D. & Chalupova, M. Technology for the preparation of PDMS optical fibers and some fiber structures. *IEEE Photon. Technol. Lett.* **26**, 1446–1449 (2014).
- Missinne, J. et al. Stretchable optical waveguides. *Opt. Express* **22**, 4168–4179 (2014).
- Harnett, C. K., Zhao, H. C. & Shepherd, R. F. Stretchable optical fibers: threads for strain-sensitive textiles. *Adv. Mater. Technol.* **2**, 1700087 (2017).
- Leber, A., Cholst, B., Sandt, J., Vogel, N. & Kolle, M. Stretchable thermoplastic elastomer optical fibers for sensing of extreme deformations. *Adv. Funct. Mater.* **29**, 1802629 (2019).

## Acknowledgements

This work is supported by the Ministry of Education Singapore (grant R-143-000-B43-114); Agency for Science, Technology and Research (A\*STAR) (grant A1983c0038); National Research Foundation, Prime Minister's Office, Singapore (CRP award no. NRF-NRFI05-2019-003 and NRF-CRP19-2017-01); National Basic Research Program of China (973 Program, grant 2015CB932200); and National Key R&D Program of China (YS2018YFB110012). We thank Yongan Tang, Zhuang Liu and Yong Zuo for their technical assistance.

## Author contributions

X.L., L.Y. and B.H. conceived and designed the project. X.L., B.Z. and R.Z. supervised the project and led the collaboration efforts. L.Y. characterized the materials and conducted the numerical simulations. C.L. completed the electrical device fabrication. B.H., L.Y. and H.Z. performed the luminescence measurements and conducted the experimental validation. B.H. and L.Y. wrote the manuscript. X.L., B.Z. and R.Z. edited the manuscript. All the authors participated in the discussion and analysis of the manuscript.

## Competing interests

The authors declare no competing interests.

## Additional information

**Supplementary information** The online version contains supplementary material available at <https://doi.org/10.1038/s41928-022-00841-8>.

**Correspondence and requests for materials** should be addressed to Bin Zhou or Xiaogang Liu.

**Peer review information** *Nature Electronics* thanks Lin Dong, Meidan Ye and the other, anonymous, reviewer(s) for their contribution to the peer review of this work.

**Reprints and permissions information** is available at [www.nature.com/reprints](http://www.nature.com/reprints).

**Publisher's note** Springer Nature remains neutral with regard to jurisdictional claims in published maps and institutional affiliations.

Springer Nature or its licensor holds exclusive rights to this article under a publishing agreement with the author(s) or other rightsholder(s); author self-archiving of the accepted manuscript version of this article is solely governed by the terms of such publishing agreement and applicable law.

© The Author(s), under exclusive licence to Springer Nature Limited 2022